THE JOURNAL OF PHYSICAL CHEMISTRY C

Article

pubs.acs.org/JPCC

Rapid Screening by Scanning Electrochemical Microscopy (SECM) of Dopants for Bi_2WO_6 Improved Photocatalytic Water Oxidation with Zn Doping

Chinmoy Bhattacharya,[†] Heung Chan Lee, and Allen J. Bard*

Center for Electrochemistry, Department of Chemistry and Biochemistry, The University of Texas at Austin, 105 E. 24th Street, Stop A5300, Austin, Texas 78712, United States

Supporting Information

ABSTRACT: Bi_2WO_6 microelectrode arrays on FTO glass substrates were fabricated by a picoliter solution dispensing technique using $Bi(NO_3)_3$ as the Bi source and $(NH_4)_6H_2W_{12}O_{40}$ as the W source in ethylene glycol. The scanning electrochemical microscope modified by using an optical fiber in place of an ultramicroelectrode was employed for rapid screening of the Bi_2WO_6 arrays and to investigate the effect of 12 different dopants on the photocatalytic oxidation of SO_3^{2-}. Among the different dopant compositions, addition of 12% Zn showed a photocurrent enhancement of up to 80% compared with that of the pure Bi_2WO_6. This result was further confirmed with bulk electrode studies for SO_3^{2-} and water oxidation. UV–vis absorption, electrochemical impedance spectroscopy, scanning electron microscopy, and X-ray diffraction studies were carried out with the photocatalysts to elucidate the role of Zn in the bulk semiconductors. Absorbed photon-to-current efficiency and incident photon-to-current efficiency determinations further confirm the enhancement of photoelectrochemical behavior upon addition of Zn to Bi_2WO_6 photocatalysts.

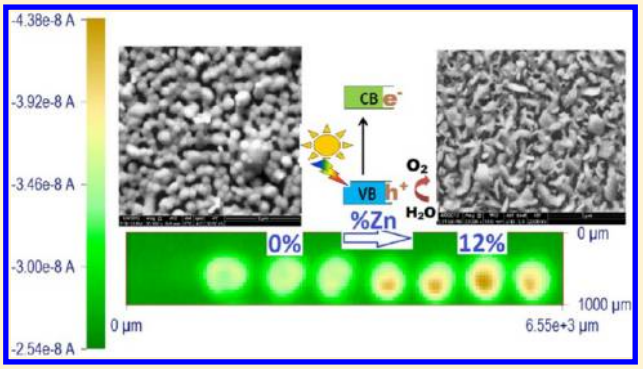

INTRODUCTION

The present study describes the preparation and rapid screening of microelectrode arrays of Bi_2WO_6 using scanning electrochemical microscopy (SECM) to find suitable dopants for better photoelectrochemical (PEC) performance of the semiconductor. When 12% Zn was introduced as a dopant to the Bi_2WO_6, the photocatalytic current of the semiconductor (SC) increased significantly. Photocatalyst-based semiconductor–liquid junction solar cells are now considered a promising route for harvesting chemical energy directly from sunlight, and a large number of candidate materials have been investigated.[1] In PEC cells, a semiconductor is excited by light of energy higher than the band gap, which results in formation of electron–hole pairs. These are separated in the electric field at the interface with the liquid and drive a heterogeneous electron-transfer reaction. Photocatalysis has attracted much attention during recent years due to its potential to split water into H_2 and O_2 as well as for environmental purification through photodecomposition of different waste materials, dyes, polymers, and sterilization of bacteria.[2−5] TiO_2 is one of the most widely explored photocatalyst materials due to its high stability, nonpolluting nature, and low cost.[6] However, the large band gap, E_g, of TiO_2 [E_g = 3.2 eV (anatase) and 3.0 eV (rutile)] limits its efficiency with solar wavelengths, and extensive investigations continue to uncover suitable semiconductor materials with more appropriate band gaps to harvest more of the visible as well as in the near UV region of the solar spectrum. For example, binary and ternary semiconductor oxides, for example, $BiVO_4$,[7,8] Ag_3PO_4,[9] Ag_3VO_4,[10] and many others, have been suggested for PEC applications.

Bi_2WO_6, a member of the "Aurivillius" family of bismuth-based mixed oxides,[11] represented by the general formula of $(Bi_2O_2)^{2+}[A_{m-1}B_mO_{3m+1}]^{2-}$ (for Bi_2WO_6, A = Bi, B = W, and m = 1), are known to form layered structures consisting of the regular intergrowth of $[A_{m-1}B_mO_{3m+1}]^{2-}$, that is, $(WO_4)^{2-}$ perovskite-like slabs and $(Bi_2O_2)^{2+}$ sheets. This group of compounds comprises some important ferroelectric materials and oxide anion conductors. In particular, Bi_2WO_6 oxide has attracted a great deal of attention due to its significant piezoelectric behavior, catalytic activity, and nonlinear dielectric susceptibility.[12−15] The layered structure of this compound has been reported to make it suitable for charge-transfer processes because of restricted recombination of the photogenerated holes and electrons.[16] However, most of the research has concentrated on the photocatalytic activity of Bi_2WO_6 "particles" toward the photodecomposition of dyes or other organic molecules and with a quite low PEC performance even in the presence of sacrificial reagents. This semiconductor photocatalyst has been primarily synthesized through solid-state reactions,[11] the hydrothermal route,[17−20] or by coprecipitation

Received: August 30, 2012
Revised: March 26, 2013
Published: April 10, 2013

techniques.[21] These are often difficult to control to obtain the desired stoichiometry and to incorporate other elements as dopants for further modification of its properties.

In the present study, we report a rapid and effective approach to synthesize thin films and arrays of Bi_2WO_6 using a drop-casting technique of solutions of simple precursor salts of the individual metal elements. The effect of the dopant for Bi_2WO_6 was determined by rapid screening with the SECM technique of the microelectrode arrays; these results were further confirmed through measurement of PEC performance of larger electrodes by linear sweep voltammetry (LSV), photocurrent spectra measurements, and calculation of the incident photon-to-current efficiency (IPCE) and absorbed photon-to-current efficiency (APCE). UV−visible absorption, electrochemical impedance spectra (EIS), X-ray diffraction (XRD), and scanning electron microscopy (SEM) characterization was employed for physical and surface characterization of the doped Bi_2WO_6 to help understand the role of dopant in the change of the performance of the materials.

EXPERIMENTAL SECTION

Materials. All the chemicals, namely, $Bi(NO_3)_3{\cdot}5H_2O$, $(NH_4)_6H_2W_{12}O_{40}{\cdot}xH_2O$ (Sigma-Aldrich), Na_2SO_4, Na_2SO_3, and ethylene glycol (EG) (Fisher Scientific) were purchased commercially and used as-received. All metal precursor solutions were prepared in ethylene glycol at a 0.1 M concentration. Milli-Q water was used to prepare aqueous solutions for electrochemistry experiments. F-doped tin oxide (FTO)-coated glass (~30 Ω/sq, Pilkington, Toledo, OH) was used as a substrate and cut into 1.5 cm × 2.0 cm pieces to prepare photocatalyst arrays and thin films as bulk electrodes.

Preparation of Bi_2WO_6 Semiconductor Photocatalyst Arrays on FTO Glass. A picoliter solution dispenser (model 1550, CH Instruments, Austin, TX) was used to fabricate the photocatalyst arrays. It consists of a computer-controlled stepper-motor-operated XYZ stage with a piezoelectric dispensing tip (MicroJet AB-01-60, MicroFab, Plano, TX) attached to the head and a sample platform. The arrays were prepared by a previously reported procedure.[11] In general, the FTO glass substrate was placed on the sample platform of the dispenser and the XYZ stage moved the tip in a preprogrammed pattern, while the metal precursor solution (in ethylene glycol) was dispensed dropwise by applying voltage pulses. The first metal precursor solution (0.1 M in ethylene glycol) was loaded and dispensed in a predesigned pattern onto the FTO, and after washing the tip, the second and third components, 0.1 M in ethylene glycol, respectively, were loaded and dispensed. Each spot has a total of 33 drops with a size of <600 μm in diameter, and the spot composition was determined by the relative number of drops of each precursor solution. The prepared arrays were annealed at 650 °C for 3 h in air with a heating rate of 1 °C/min, which produced the desired oxide materials.

Screening of the Arrays. The screening of the photocatalyst arrays was performed by an optical-fiber-modified SECM setup described in a previous publication.[7] Briefly, a 400 μm optical fiber (FT-400-URT, 3M, St. Paul, MN) attached to a 150 W xenon lamp was used in place of a UME and connected to the tip holder of a CHI model 900B SECM instrument. The prepared photocatalyst array was placed in a Teflon cell with an O-ring (exposed area: 1.0 cm^2). A Pt wire counter electrode and a Ag/AgCl reference electrode were used in 0.1 M Na_2SO_4 electrolyte with 0.1 M Na_2SO_3. The optical fiber was positioned perpendicular to the array surface at a 100 μm distance and scanned across the surface at 500 μm/s. During the scan, a potential of 0.2 V (vs Ag/AgCl) was applied to the working electrode array by the SECM potentiostat. The measured photocurrent during the scan produced a color-coded two-dimensional image. From the SECM image, the most intense spot in the arrays was selected as the most suitable material for PEC applications in the form of a bulk electrode.

Preparation and Photoelectrochemical Measurements of Bulk Samples. Premixed solutions containing 10 mM Bi and 5 mM W along with 0.6 mM Zn (for 12% Zn-doped Bi_2WO_6 film) in ethylene glycol were prepared, and 300 μL of the precursor solution was drop-cast onto the FTO substrate (1.5 × 2.0 cm), followed by annealing at 650 °C for 3 h in air in the same manner as the array sample preparation. The resulting thin film was used as a working photoelectrode with a 0.27 cm^2 geometric area exposure (using one O-ring of the same inner area) to the electrolyte solution under light irradiation. All electrochemical experiments were carried out in a borosilicate glass cell using a three-electrode configuration with a Pt-foil counter electrode and a Ag/AgCl reference electrode, using a CHI potentiostat (model 630, CH Instruments, Austin, TX). Light irradiation was performed through the electrolyte solution by a Xe arc lamp (Oriel, 150 W) with an incident beam intensity of 100 mW/cm^2. The PEC measurements were carried out either in 0.1 M Na_2SO_4 with 0.1 M Na_2SO_3 as a sacrificial electron donor or in 0.1 M Na_2SO_4 alone for water oxidation. The pH of the aqueous solution used for water oxidation was maintained at 7 using 0.1 M phosphate buffer solution. To study the responsiveness of the semiconductors toward photooxidation of either water or SO_3^{2-} under visible illumination, a UV cutoff filter (λ > 420 nm) was placed in front of the Xe lamp. A monochromator (Oriel) was used to obtain the action spectrum and a power meter (Newport, model 1916-C) and a silicon detector (Newport, model 818-UV) to measure the power of the light.

Characterization. The surface morphology of the Bi_2WO_6 thin film electrode with and without Zn doping was characterized with a scanning electron microscope (SEM, Quanta 650 FEG, FEI Company, Inc., Hillsboro, OR). XRD measurements were carried out to identify the crystalline phases of the films using a D8 ADVANCE instrument (Bruker, Fitchburg, WI) equipped with a Cu Kα radiation source operated at 40 kV and 40 mA with a scan rate of 12°/min in the 2θ range of 20−90°. The thickness of the drop-cast films was measured using a Veeco NT9100 Optical Profiler. A portion of the films was scratched off gently to expose the bare FTO glass, and the FTO−semiconductor boundary region was subjected to an optical profilometer. UV−visible absorption spectroscopy measurements were performed with a Milton-Ray spectrophotometer (Model Spectronic 3000 ARRAY) in the range of 310−800 nm using the thin films of both materials.

Absorption coefficients (α) were calculated to obtain the Tauc plot[22] for the semiconductor materials to find the band gap as well as the nature of the semiconductor (i.e., direct or indirect band gap). The absorption coefficient, α, which is independent of film thickness (z), was obtained from the thickness-normalized absorbance value (A_λ) at different wavelengths (eq 1).

$$\alpha = -\ln(10^{-A_\lambda})/z \quad (1)$$

EIS was performed using an Autolab instrument (PGSTAT302/FRA2). Impedance measurements were carried

dx.doi.org/10.1021/jp308629q | J. Phys. Chem. C 2013, 117, 9633−9640

out in 0.1 M Na_2SO_4 aqueous solution with an exposed surface area of 1 cm^2 and using a frequency of 200, 500, and 1000 Hz with an ac amplitude of 5 mV at each potential.

RESULTS AND DISCUSSION

To improve the photocatalytic activity of Bi_2WO_6 semiconductors, different third elements were introduced in the microelectrode arrays through the pL solution dispensing technique. The incorporation of a new metallic element within the semiconductor matrix can affect its overall photocatalytic behavior in different ways. Among these, the important factors considered are (i) formation of a new material along with the original matrix, (ii) replacement of the original lattice sites of the primary elements with dopant elements, and (iii) incorporation of dopants in interstitial positions of the crystal lattice. These structural and chemical changes can result in (i) modification of the band edges of the main semiconductor, (ii) formation of some intermediate bands, (iii) introduction of recombination sites for the photoexcited electron–hole pairs, (iv) change in the carrier concentration either in the valence band or in the conduction band, and (v) change in the carrier mobility.

Screening of the Microelectrode Arrays. In the present study, we have tried different dopant elements, such as Zn, Co, V, Sr, Cu, Ni, Cr, Fe, Ag, Mo, Ca, and Ta. Among all of these, only Zn showed significant enhancement of photoactivity when incorporated at an optimum level of 12% to the matrix. Figure 1 represents the SECM image of the Bi_2WO_6 arrays doped with

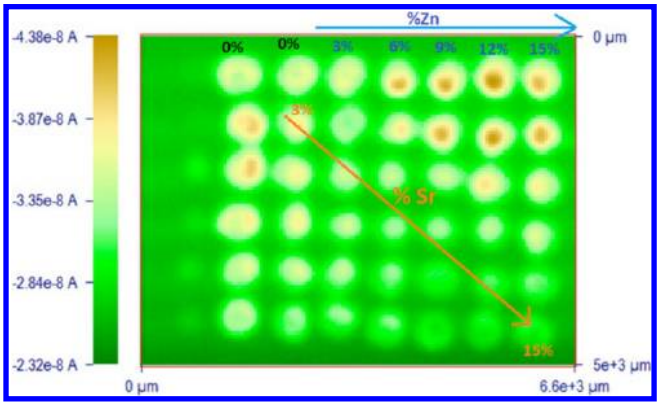

Figure 1. SECM images of the spot array of Zn- and Sr-doped Bi/W oxide photocatalysts in a 0.1 M Na_2SO_3/Na_2SO_4 solution with the array held at the constant applied potential of 0.2 V (vs Ag/AgCl reference electrode) under UV–visible light. The Zn concentration increased in 3% steps in the horizontal direction, and the Sr concentration increased in 3% steps in the diagonal direction.

different levels of Zn and Sr, when the substrate is held at a constant potential of 0.2 V (vs Ag/AgCl reference electrode). The spot corresponding to 12% Zn shows an enhanced photocurrent of about 1.8 times higher than that of the undoped Bi_2WO_6 material under exposure to UV–visible light. Sr, Ta, Cu, Ni, Ca, Cr, Ag, and Mo showed very small or insignificant changes in the photocurrent, and Co, V, and Fe decreased the photoactivity of the base material. Typical results using these dopants are presented in the Supporting Information (Figure S1a–e). Figure 1 clearly shows that an increase in Zn level in the matrix improves the behavior of the material toward photooxidation of SO_3^{2-}. This effect increased gradually with the amount of Zn and reached a maximum at a level of 12% Zn; there was a decrease in its photocurrent with a further increase in Zn content.

Bulk Film Study. After selecting the optimized concentration of the suitable dopant (12% Zn into Bi_2WO_6 matrix), we prepared Bi_2WO_6 bulk film electrodes on FTO glass substrates with and without Zn doping and characterized them through PEC measurements. The PEC behavior of these materials was studied under full UV–visible illumination using a 150 W xenon lamp source with periodic chopping of the incident light for either water oxidation, that is, in the presence of 0.1 M Na_2SO_4 alone, or oxidation of the sacrificial reagent, that is, 0.1 M Na_2SO_3 in the presence of 0.1 M Na_2SO_4. Figure 2a depicts the LSVs of Bi_2WO_6 and 12% Zn-doped Bi_2WO_6

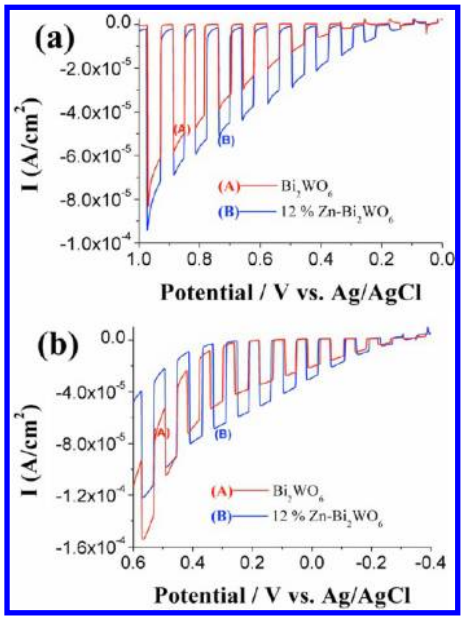

Figure 2. LSVs of Bi_2WO_6 and 12% Zn-doped Bi_2WO_6 thin films in (a) 0.1 M SO_4^{2-} and (b) 0.1 M SO_3^{2-} with 0.1 M SO_4^{2-} solution under chopped UV–visible illumination (intensity: 100 mW/cm^2).

bulk electrodes in 0.1 M Na_2SO_4 solution at a scan rate of 20 mV/s in the potential range of 0–1.0 V vs Ag/AgCl; on this scale, water oxidation thermodynamically occurs at about 0.7 V. Figure 2b represents the LSV plot of the same materials in the presence of 0.1 M Na_2SO_3 along with 0.1 M Na_2SO_4 in the potential range of −0.4 to 0.6 V vs Ag/AgCl. In Figure 2a, the photocurrent onset potential is shifted more negative by 150 mV with Zn-doping, indicating a more facile photocatalytic water oxidation process on that surface, whereas for SO_3^{2-} oxidation, both materials show almost identical behavior. This suggests that Zn-doping does not cause a significant band shift, but rather appears to promote the water oxidation reaction. The enhancement of the photocurrent at 0.2 V (vs Ag/AgCl) in both the cases was comparable to that recorded in SECM measurements using the microelectrode arrays. The photocurrent values for water oxidation in Figure 2a were smaller in magnitude than those with a sacrificial donor (Figure 2b) because of the slower kinetics of water oxidation as compared to that for the photooxidation of SO_3^{2-}. Moreover, the nonideal shape of the current–potential curve, that is, a low fill factor for water oxidation (Figure 2a), also indicates slower water oxidation kinetics. On the other hand, idealized current–potential plots confirmed an improved fill-factor parameter for photooxidation of SO_3^{2-} (Figure 2b) and can be explained

dx.doi.org/10.1021/jp308629q | J. Phys. Chem. C 2013, 117, 9633–9640

through more facile charge transfer at this semiconductor surface.

The response to visible illumination was obtained with a 420 nm cutoff filter in front of the xenon lamp. The LSVs corresponding to the PEC water and sacrificial SO_3^{2-} oxidation are shown in Figure 3 and the Supporting Information (Figure S2a,b). The higher photoresponse of the Zn-doped film under visible light illumination as compared to that of the undoped Bi_2WO_6 film indicates better absorption of the doped material in the visible region. The LSVs of the Zn-doped materials under visible illumination resemble the trend of full UV−visible illumination, although the activity of the photocatalysts decreased significantly because of the smaller absorbance in the visible region.

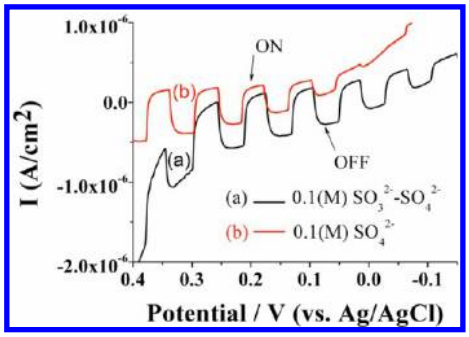

Figure 3. LSVs of the 12% Zn-doped Bi_2WO_6 thin films in 0.1 M SO_4^{2-} and 0.1 M SO_3^{2-} with 0.1 M SO_4^{2-} solution under chopped visible light.

To evaluate the stability to the material toward water photooxidation, continuous photocurrent measurements were carried out for 1 h in 0.1 M Na_2SO_4 solution when the electrode was held at a fixed potential of 0.8 V vs Ag/AgCl under the constant illumination of 100 mW/cm^2. The chronoamperometry curves, as shown in Figure 4, demonstrate that both films are quite stable under these conditions. During the long-term stability test, bubbles were clearly observed, as shown in the Supporting Information (Figure S3).

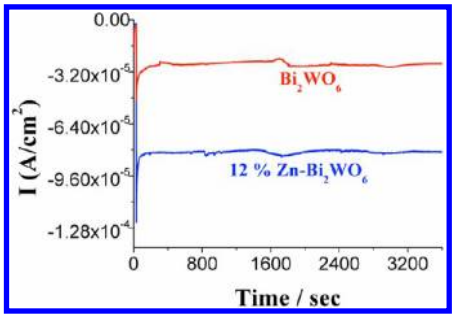

Figure 4. Photocurrent vs time (stability test) of Bi_2WO_6 and 12% Zn-doped Bi_2WO_6 thin films in 0.1 M SO_4^{2-} solution under UV−visible light illumination (intensity: 100 mW/cm^2). Constant applied potential of 0.8 V vs Ag/AgCl reference electrode.

The uniformity of the drop-cast films was characterized by optical profilometry. Figure S4a (Supporting Information) shows the optical image. The height difference across the FTO to the SC thin film (i.e., the Y profile) as obtained from the associated analysis software yields a thickness of the SC film as 500 ± 10 nm (Supporting Information, Figure S4b). The optical image and the thickness profile diagram suggest a fairly uniform film with only small defects.

UV−visible absorption measurements were performed on the as-prepared thin films to calculate the band-gap energies and to find out the nature of the bands. Figure 5a shows the UV−visible spectra of the undoped and 12% Zn-doped Bi_2WO_6 semiconductor thin films. The UV−vis spectra indicate the improvement to the solar absorption properties, including the visible light region when 12% Zn is added to Bi_2WO_6. The steep shape of the UV−vis spectra confirms that the absorption of suitable energy photons was primarily due to band-to-band transition. The variation of the absorption coefficient parameters $[(\alpha h\nu)^2]$, as calculated from the absorption spectra, at different photon energies ($h\nu$) is presented as a Tauc plot (Figure 5b (inset)). The band gap (taken as the optical gap) of a Bi_2WO_6 bulk material, as calculated from the intercept of the extended linear portion of the Tauc plot, is 3.3 eV, whereas addition of 12% Zn to the matrix reduces the band gap to 3.1 eV. The enhanced photocatalytic oxidation properties of the Zn-doped Bi_2WO_6 over the undoped material, as observed in the LSV plots, can be attributed to the smaller band-gap energy, increased absorptivity of the Zn-doped material, and their favorable morphology, as discussed later in the SEM analysis section.

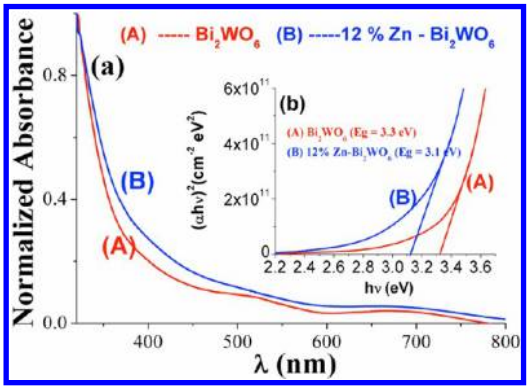

Figure 5. (a) Normalized UV−visible absorbance spectrum for Bi_2WO_6 and 12% Zn-doped Bi_2WO_6 thin films. (b) Tauc plot for the Bi_2WO_6 and 12% Zn-doped Bi_2WO_6 thin films for calculation of the optical band gap of the semiconductors.

Finally, the action spectrum for the semiconductor−electrolyte interface was recorded through chronoamperometry with a change in the monochromatic wavelength from deep UV to the visible region (250−500 nm), and the corresponding photocurrent spectra versus wavelength were calculated. IPCE was determined by further measuring the power of the incident beam of light at specified wavelengths. IPCE describes the ratio of "effective photons" or generated charges that generate electrochemical current at the semiconductor electrolyte interface to "incident photons" of monochromatic light. It is calculated as a function of output photocurrent density (I_{ph}, A/cm^2) and incident light power density (P_{in}, W/cm^2) at each wavelength λ (nm) as given by eq 2. On the other hand, the APCE is determined by the portion of actual "absorbed photons" by the semiconductor. The relation between IPCE and APCE is shown in eq 3, where the A corresponds to the absorbance of the material, as measured through UV−vis spectra.

$$\mathrm{IPCE}(\%) = [\{(I_{ph}\ (\mathrm{A/cm^2})/P_{in}\ (\mathrm{W/cm^2})\}\{1240/\lambda\ (\mathrm{nm})\}]100 \qquad (2)$$

dx.doi.org/10.1021/jp308629q | J. Phys. Chem. C 2013, 117, 9633−9640

$$\mathrm{APCE}(\%) = [\mathrm{IPCE}/(1 - 10^{-A})] \quad (3)$$

Figure 6a represents the action spectrum of the two materials for water oxidation (in 0.1 M Na_2SO_4 solution) at 0.8 V vs Ag/AgCl reference electrode under monochromatic illumination. Figure 6b (inset) is the representation of the chronoamperometric diagram with chopped monochromatic light at different wavelengths ranging from 270 to 450 nm, for the two materials in 0.1 M SO_4^{2-} solutions holding at a constant potential of 0.8 V vs Ag/AgCl reference electrode. The corresponding IPCE and APCE, as derived from the respective photocurrent density at each wavelength, using eqs 2 and 3, are presented in Figure 7. The small difference in the IPCE and APCE plots results from the rather thick films employed and high light absorption. The wavelength-dependent photocurrent measurement is informative in highlighting the difference of the relevant band edges of the semiconductors. The onset of photocurrent for the 12% Zn-doped material is shifted toward longer wavelength compared with that of the undoped Bi_2WO_6 material, which is suggestive of a decrease of the band gap of the Zn-doped semiconductor. The IPCE and APCE data are also supportive of the above results. The maximum value of IPCE for the Zn-doped materials is 28.1% and the corresponding APCE value is 28.9%, whereas for the undoped material, the highest obtained IPCE was 7.2% and APCE was 8.2%. The significant enhancement of the photon-to-current conversion efficiencies with the Zn-doped Bi_2WO_6 semiconductor can be attributed to the modified band structure as well as favorable bulk and surface properties (in terms of crystalline behavior and surface morphology, discussed later).

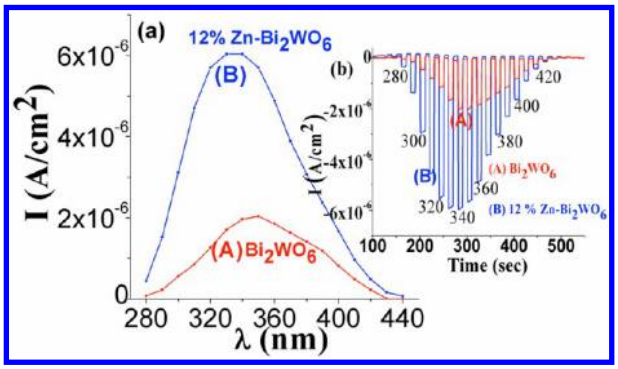

Figure 6. (a) Action spectrum of Bi_2WO_6 and 12% Zn-doped Bi_2WO_6 thin films in 0.1 M SO_4^{2-} solution. Constant applied potential of 0.8 V vs Ag/AgCl reference electrode. (b) Chronoamperometry plots with chopped monochromatic light at different wavelengths for the two materials in 0.1 M SO_4^{2-} solutions to derive the action spectrum.

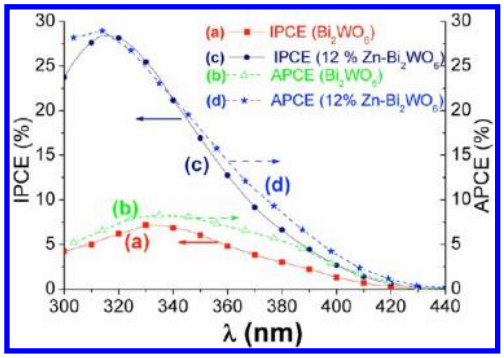

Figure 7. IPCE and APCE plots of Bi_2WO_6 and 12% Zn-doped Bi_2WO_6 thin films in 0.1 M SO_4^{2-} solution at applied potential of 0.8 V vs Ag/AgCl reference electrode.

To support the above observations, the same experiments were carried out at a lower potential, 0.3 V vs Ag/AgCl, and the corresponding action spectra and chronoamperometry diagram under monochromatic chopped light are shown in the Supporting Information as Figure S5a,b. The IPCE and APCE plots derived from the photocurrent spectra are also shown (Supporting Information, Figure S6). The application of a much lower potential compared to that of the thermodynamic water oxidation potential value results in a decrease in the photocurrents and the corresponding IPCE and APCE values. However, the overall trends in all the estimated parameters are the same as those performed at higher potential (at 0.8 V vs Ag/AgCl).

The thin films were subjected to EIS to determine the flat-band potentials. Experiments were carried out in 0.1 M Na_2SO_4 solution at different frequencies (200, 500, and 1000 Hz) within the potential region of −0.8 to 0.1 V vs Ag/AgCl. The Mott−Schottky (M-S) plot,[23] the linear variation of C^{2-} with respect to the applied potential, follows the relation shown in eq 4

$$C^{-2} = [2/(\varepsilon_s \varepsilon_0 e N_D)][E - E_{fb} - (k_B T/e)] \quad (4)$$

where C is the interfacial capacitance, ε_s is the dielectric constant of the semiconductor, ε_0 is the permittivity of free space, e is the electronic charge, N_D is the donor density, E is the applied potential, E_{fb} is the flat band potential, k_B is the Boltzmann constant, and T is the absolute temperature. The flat band potential of the semiconductor−electrolyte interface can be obtained from the intercept on the potential axis, whereas the slope of the straight line is related to the carrier concentration. Figure 8a,b shows typical M-S plots for the undoped and 12% Zn-doped Bi_2WO_6 semiconductor in the water oxidation system. The positive slope of the M-S plots confirms the n-type semiconductivity for both of the materials. The estimated flat band potentials are −0.8 V (vs Ag/AgCl) for both the Bi_2WO_6 and Zn-doped Bi_2WO_6 with a considerable uncertainty of ±0.05 V, which is usual for a Mott−Schottky experiment. The donor density of Bi_2WO_6 as calculated from the slope of the respective M-S plots, taking the dielectric constant (ε_s) as 200 for Bi_2WO_6,[24] is found to be of the order of $1.4 \times 10^{19}/\mathrm{cm}^3$, which is similar to values reported for the other semiconductor materials, such as ZnO[25] and TiO_2[26], in photocatalytic experiments. For the Zn-doped Bi_2WO_6 semiconductor, since the slope of the Mott−Schottky plot was found to be of the same order to that of the undoped semiconductor, the donor density of the semiconductors remained unaffected with Zn-doping. The similar trend in the slope of the graphs may be estimated from the individual Mott−Schottky plots.

SEM reveals the quality of the films as well as their surface morphology. Figure 9a shows the SEM image of the undoped Bi_2WO_6 film with uniformly distributed spherical particles of ∼400 nm in diameter. On addition of Zn, the SEM image (Figure 9c) revealed that the surface morphology changes to some extent with the growth of flakelike crystallites with an average size of 550 nm by 150 nm, along with the regular spherical particles. The as-deposited films were uniform and free from any major cracks or large bumps, as shown at lower magnification (×1000) (Figure 9b,d (insets)).

dx.doi.org/10.1021/jp308629q | J. Phys. Chem. C 2013, 117, 9633−9640

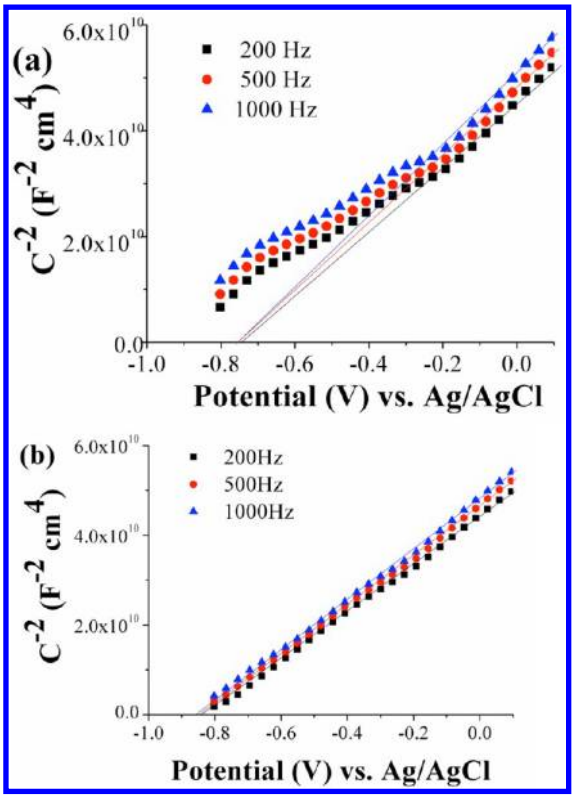

Figure 8. Mott–Schottky plots for (a) Bi_2WO_6 and (b) 12% Zn-doped Bi_2WO_6 thin films in 0.1 M Na_2SO_4 solution.

XRD measurements were carried out on the bulk film electrodes to determine the nature of crystallites grown with both materials. The diffraction pattern of undoped Bi_2WO_6 (Figure 10a) indicates that the material is highly crystalline in nature and matches that of the reference material "Russellite", γ-Bi_2WO_6 (orthorhombic phase), and the different XRD peaks were indexed using JCPDS data file 39-0256. On addition of 12% Zn to the Bi_2WO_6 matrix, the XRD plot (Figure 10b) shows an almost identical pattern to that of the pure material. The peak at 28.38° remains the strongest peak (~100%) for both the materials corresponding to the (1,1,3) phase of the crystallites. When comparing the XRD patterns of undoped Bi_2WO_6 with Zn-Bi_2WO_6 film, we found some low-intensity peaks corresponding to 2θ values at 27.36, 29.33, 31.40, 34.20, and 36.08°. These peaks were identified as different cubic forms of Bi_2O_3 and hexagonal ZnO and are shown in Figure 10c (inset).

To confirm the effect of Zn on the crystalline behavior of the Bi_2WO_6 matrix, different levels of Zn (2, 8, 12, and 18%) were added to the semiconductor matrix, and the respective XRD patterns are presented in the Supporting Information (Figure S7). The XRD plots of all the materials show that addition of different levels of Zn did not affect the crystalline pattern of the Bi_2WO_6 matrix, since the relative intensities of the individual peaks as well as their absolute positions (2θ values) remained unchanged. However, for the Zn-Bi_2WO_6 materials, appearance of the small peaks due to Bi_2O_3 suggests that Zn effectively substitutes for Bi lattice sites without changing the crystalline parameters of the main Bi_2WO_6 structure.

The lack of variation of the XRD pattern for the crystallinity of Bi_2WO_6 in the Zn-added films in relation to the changed band-gap energies may be explained in different ways. (i) A small amount of Zn substitutes the Bi in lattice sites up to a certain level without changing the crystal structure of the main Bi_2WO_6 lattice, leading to release of Bi^{3+} ions in the form of Bi_2O_3, as detected in the XRD analysis. (ii) This Zn

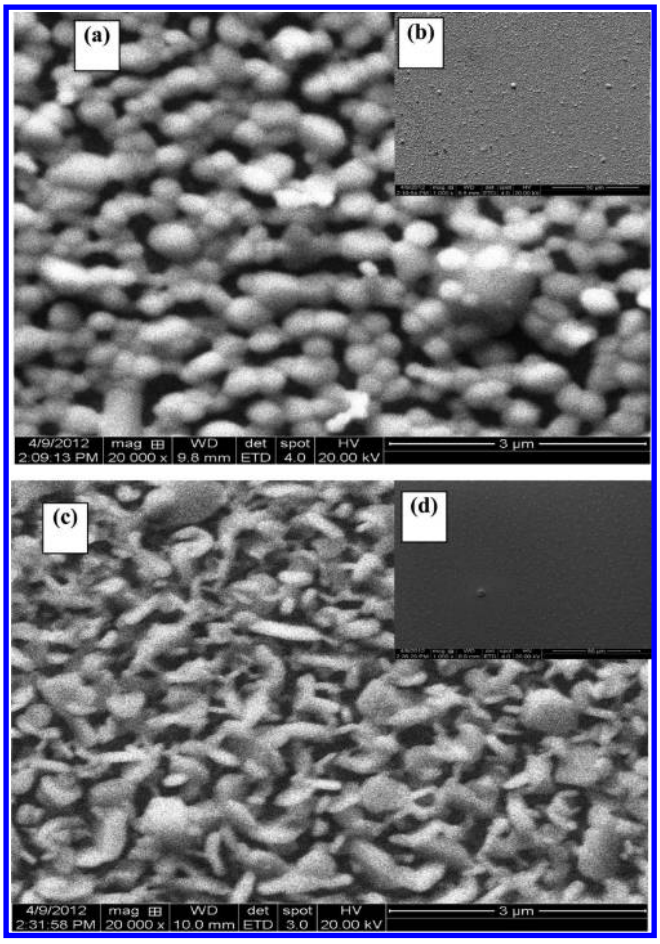

Figure 9. SEM image of the (a) Bi_2WO_6 and (c) 12% Zn-doped Bi_2WO_6 thin films at higher magnification (×20 000). Insets: (b) and (d) are the respective SEM images at lower magnification (×1000) to verify the uniformity of the deposited films.

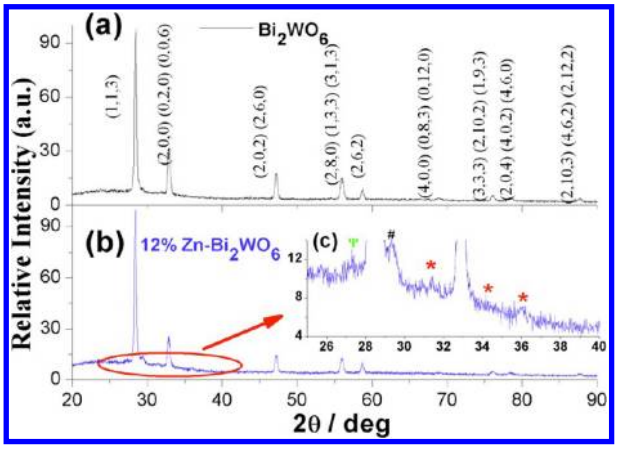

Figure 10. XRD pattern of the (a) Bi_2WO_6 and (b) 12% Zn-Bi_2WO_6 thin films. The peaks were indexed using JCPDS data file 39-0256 (γ-Bi_2WO_6, orthorhombic phase), and are marked. (c) The magnified area of the Zn-Bi_2WO_6 XRD pattern showing low-intensity peaks corresponding to Bi_2O_3 and ZnO. The different peaks marked as: ψ, $Bi_2O_3^{cubic}$ (index number: 16-0654); #, $Bi_2O_3^{cubic}$ (index number: 65-3319); *, $ZnO^{hexagonal}$ (index number: 36-1451).

dx.doi.org/10.1021/jp308629q | J. Phys. Chem. C 2013, 117, 9633–9640

substitution into the matrix forms an intermediate band (intraband) structure, leading to decrease of band-gap energy to a small extent (~0.2 eV), as observed in the UV−vis measurements and through action spectra. (iii) Some portion of added Zn incorporates into interstitial positions of the "Aurivillius" structure on a "random" basis and, therefore, is not detected in the XRD studies. This type of behavior has also been observed in other studies.[27−29] (iv) The remaining portion of added Zn (above that substituted for Bi and interstitial), remains as ZnO (v) The presence of ZnO in the matrix might lead to different surface morphologies, as observed through SEM analysis, favorable for the PEC oxidation process forming a more compact surface structure.

CONCLUSIONS

In the present study, we have demonstrated the application of scanning electrochemical microscopy (SECM) for rapid screening of Bi_2WO_6-based photocatalysts and found that Zn as a dopant enhances the PEC behavior of the base material. Addition of Zn to an optimum level of 12% leads to an increase in the performance of the photocatalyst arrays by 1.8 times over that of the undoped material at 0.2 V vs Ag/AgCl, under UV−visible illumination for both SO_3^{2-} and water oxidation. This same PEC enhancement was further verified through experiments with bulk electrodes prepared by the drop-casting technique. Thickness profile measurement confirms the uniform nature of the ~500 nm films as grown on FTO glass. The onset of PEC behavior in the near-UV region and UV−vis absorption spectra demonstrate that the band gap of the undoped Bi_2WO_6 is 3.3 eV, whereas that modified with Zn was 3.1 eV. XRD analysis shows homogeneous mixing of Zn into the Bi_2WO_6 matrix without changing the crystallinity of the Bi_2WO_6 matrix. SEM analysis showed modification of the surface structure of the 12% Zn-doped Bi_2WO_6 photocatalyst.

ASSOCIATED CONTENT

Supporting Information

Scanning photoelectrochemical microscopy (SPECM) images of Co/V-, Cu/Ni-, Cr/Fe-, Ag/Mo-, and Ca/Ta-doped Bi_2WO_6 semiconductor arrays, LSV plots of the materials in 0.1 M SO_4^{2-} and 0.1 M SO_3^{2-}−SO_4^{2-} solution under visible light illumination, Veeco thickness profile images, action spectrum and IPCE-APCE plots in 0.1 M SO_4^{2-} solution at 0.3 V, and XRD pattern of the different levels of Zn added Bi_2WO_6 films. This material is available free of charge via the Internet at http://pubs.acs.org.

AUTHOR INFORMATION

Corresponding Author

*E-mail: ajbard@mail.utexas.edu. Phone: 512-471-3761. Fax: 512-471-0088.

Present Address

[†]BOYSCAST Fellow (DST, Govt. of India), Department of Chemistry, Bengal Engineering & Science University, West Bengal, India (permanent address).

Notes

The authors declare no competing financial interest.

ACKNOWLEDGMENTS

The support of the Department of Energy Division of Chemical Sciences, Geosciences, and Biosciences Office of Basic Energy Science of the U.S. Department of Energy through Grant DE-FG02-09ER16119, and the Robert A. Welch Foundation (F-0021) is gratefully acknowledged. Financial support from the Department of Science Technology, Government of India, under the BOYSCAST Fellowship scheme to C.B. (File No. SR/BY/C-10/10, dated 09th May 2011), and from the Oronzio and Niccolo De Nora Foundation to H.C.L. is gratefully acknowledged. We also thank Dr. Sung Ki Cho for the SEM characterization, Dr. Kevin Leonard for helping in the thickness profile measurement, and Hyun Seo Park for useful discussions on XRD pattern analysis of the semiconductors.

REFERENCES

(1) Kudo, A.; Miseki, Y. Heterogeneous Photocatalyst Materials for Water Splitting. *Chem. Soc. Rev.* **2009**, *38*, 253−278.

(2) Walter, M. G.; Warren, E. L.; McKone, J. R.; Boettcher, S. W.; Mi, Q.; Santori, E. A.; Lewis, N. S. Solar Water Splitting Cells. *Chem. Rev.* **2010**, *110*, 6446−6473.

(3) Hoffmann, M. R.; Martin, S. T.; Choi, W.; Bahnemannt, D. W. Environmental Applications of Semiconductor Photocatalysis. *Chem. Rev.* **1995**, *95*, 69−96.

(4) Robertson, P. K. J.; Bahnemann, D. W.; Robertson, J. M. C.; Wood, F. Photocatalytic Detoxification of Water and Air. In *The Handbook of Environmental Chemistry*; Boule, P., Bahnemann, D. W., Robertson, P. K. J., Eds.; Environmental Photochemistry Part II; Springer: Berlin, 2005; Vol. *2M*, pp 367−423.

(5) Lianos, P. Production of Electricity and Hydrogen by Photocatalytic Degradation of Organic Wastes in a Photoelectrochemical Cell: The Concept of the Photofuelcell: A Review of a Re-emerging Research Field. *J. Hazardous Mater.* **2011**, *185*, 575−590.

(6) Honda, K.; Fujishima, A. Electrochemical Photolysis of Water at a Semiconductor Electrode. *Nature* **1972**, *238*, 37−38.

(7) Lee, J.; Ye, H.; Pan, S.; Bard, A. Screening of Photocatalysts by Scanning Electrochemical Microscopy. *J. Anal. Chem.* **2008**, *80*, 7445−7450.

(8) Park, H. S.; Kweon, K. E.; Ye, H.; Paek, E.; Hwang, G. S.; Bard, A. J. Screening of Photocatalysts by Scanning Electrochemical Microscopy. *J. Phys. Chem. C* **2011**, *115*, 17870−17879.

(9) Bi, Y.; Hu, H.; Ouyang, S.; Lu, G.; Cao, J.; Ye, J. Photocatalytic and Photoelectric Properties of Cubic Ag_3PO_4 Sub-microcrystals with Sharp Corners and Edges. *Chem. Commun.* **2012**, *48*, 3748−3750.

(10) Konta, R.; Kato, H.; Kobayashi, H.; Kudo, A. Photophysical Properties and Photocatalytic Activities under Visible Light Irradiation of Silver Vanadates. *Phys. Chem. Chem. Phys.* **2003**, *5*, 3061−3065.

(11) Kudo, A.; Hijii, S. H_2 or O_2 Evolution from Aqueous Solutions on Layered Oxide Photocatalysts Consisting of Bi^{3+} with $6s^2$ Configuration and d0 Transition Metal Ions. *Catal. Lett.* **1999**, 1103.

(12) Kitaev, Y. E.; Aroyo, M. I.; Perez-Mato, J. M. Site Symmetry Approach to Phase Transitions in Perovskite-Related Ferroelectric Compounds. *Phys. Rev. B* **2007**, *75*, 064110−064120.

(13) Rae, A. D.; Thomson, J. G.; Withers, R. L. Structure Refinement of Commensurately Modulated Bismuth Tungstate, Bi_2WO_6. *Acta Crystallogr., Sect. B* **1991**, *47*, 870−881.

(14) McDowell, N. A.; Knight, K. S.; Lightfoot, P. Unusual High-Temperature Structural Behaviour in Ferroelectric Bi_2WO_6. *Chem.—Eur. J.* **2006**, *12*, 1493−1499.

(15) Islam, M. S.; Lazure, S.; Vannier, R. N.; Nowogrocki, G.; Mairesse, G. Structural and Computational Studies of Bi_2WO_6 Based Oxygen Ion Conductors. *J. Mater. Chem* **1998**, *18*, 655−660.

(16) Fu, H.; Pan, C.; Zhang, L.; Zhu, Y. Synthesis, Characterization and Photocatalytic Properties of Nanosized Bi_2WO_6, $PbWO_4$ and $ZnWO_4$ Catalysts. *Mater. Res. Bull.* **2007**, *42*, 696−706.

(17) Gui, M. S.; Zhang, W. D. Preparation and Modification of Hierarchical Nanostructured Bi_2WO_6 with High Visible Light-Induced Photocatalytic Activity. *Nanotechnology* **2011**, *22*, 265601−265609.

(18) Yu, J. G.; Xiong, J. F.; Cheng, B.; Yu, Y.; Wang, J. B. Hydrothermal Preparation and Visible-Light Photocatalytic Activity of Bi_2WO_6 Powders. *J. Solid State Chem.* **2005**, *178*, 1968−1972.

(19) Shang, M.; Wang, W. Z.; Xu, H. L. New Bi_2WO_6 Nanocages with High Visible-Light-Driven Photocatalytic Activities Prepared in Refluxing Ethylene Glycol. *Cryst. Growth Des.* **2009**, *9*, 991−996.
(20) Ng, C.; Iwase, A.; Ng, Y. H.; Amal, R. Transforming Anodized WO_3 Films into Visible-Light-Active Bi_2WO_6 Photoelectrodes by Hydrothermal Treatment. *J. Phys. Chem. Lett.* **2012**, *3*, 913−918.
(21) Alfaro, S. O.; Cruz, A. M. Synthesis, Characterization and Visible-Light Photocatalytic Properties of Bi_2WO_6 and $Bi_2W_2O_9$ Obtained by Co-precipitation Method. *Appl. Catal., A* **2010**, *383*, 128−133.
(22) Berglund, S. P.; Flaherty, D. W.; Hahn, N. T.; Bard, A. J.; Mullins, C. B. Photoelectrochemical Oxidation of Water Using Nanostructured $BiVO_4$ Films. *J. Phys. Chem. C* **2011**, *115*, 3794−3802.
(23) Bard, A. J.; Faulkner, L. R. *Electrochemical Methods Fundamentals and Application*, 2nd ed.; John Wiley & Sons: New York, 2001; pp 750−751.
(24) Sharma, V.; Varma, K. B. R.; Shukla, A. K. Structural and Dielectric Properties of a Novel Bi_2O_3-$(1 - x)WO_3 - x$CuO Solid Solution. *Bull. Mater. Soc.* **1995**, *18*, 631−636.
(25) Yang, X.; Wolcott, A.; Wang, G.; Sobo, A.; Fitzmorris, R. C.; Qian, F.; Zhang, J. Z.; Li, Y. Nitrogen-Doped ZnO Nanowire Arrays for Photoelectrochemical Water Splitting. *Nano Lett.* **2009**, *9*, 2331−2336.
(26) Baumanis, C.; Bahnemann, D. W. TiO_2 Thin Film Electrodes: Correlation between Photocatalytic Activity and Electrochemical Properties. *J. Phys. Chem. C* **2008**, *112*, 19097−19101.
(27) Chen, C. H.; Kelder, E. M.; Schoonman, J. Electrostatic Sol-Spray Deposition (ESSD) and Characterization of Nanostructured TiO_2 Thin Films. *Thin Solid Films* **1999**, *342*, 35−41.
(28) Liu, Z. L.; Cui, Z. L.; Zhang, Z. K. The Structural Defects and UV−vis Spectral Characterization of TiO_2 Particles Doped in the Lattice with Cr^{3+} Cations. *Mater. Charact.* **2005**, *54*, 123−129.
(29) Yang, S. H.; Yokoyama, M. The Effect of Li, Cu and Zn Doping on the Luminance and Conductivity of Blue $ZnGa_2O_4$ Phosphor. *Jpn. J. Appl. Phys.* **1998**, *37*, 6429−6433.